Assessing the significance of pedobarographic signals using random field theory

Todd C. Pataky

Abstract

Traditional pedobarographic statistical analyses are conducted over discrete regions. Recent studies have demonstrated that regionalization can corrupt pedobarographic field data through conflation when arbitrary dividing lines inappropriately delineate smooth field processes. An alternative is to register images such that homologous structures optimally overlap and then conduct statistical tests at each pixel to generate statistical parametric maps (SPMs). The significance of SPM processes may be assessed within the framework of random field theory (RFT). RFT is ideally suited to pedobarographic image analysis because its fundamental data unit is a lattice sampling of a smooth and continuous spatial field. To correct for the vast number of multiple comparisons inherent in such data, recent pedobarographic studies have employed a Bonferroni correction to retain a constant family-wise error rate. This approach unfortunately neglects the spatial correlation of neighbouring pixels, so provides an overly conservative (albeit valid) statistical threshold. RFT generally reduces the threshold depending on field smoothness and on the geometry of the search area, but it also provides a framework for assigning p values to suprathreshold clusters based on their spatial extent. The current paper provides an overview of basic RFT concepts and uses simulated and experimental data to validate both RFT-relevant field smoothness estimations and RFT predictions regarding the topological characteristics of random pedobarographic fields. Previously published pedobarographic data are finally re-analysed using RFT inference procedures to demonstrate how RFT yields easily understandable statistical results that may be incorporated into routine clinical and laboratory analyses.

1 Introduction

Statistical analysis of pedobarographic images has traditionally involved linear methods applied to data extracted from approximately ten anatomical regions of interest (Rosenbaum and Becker, 1997). Such approaches implicitly assume both that the regions are functionally independent and that the data are representative of the behaviour of the region from which they are extracted. There

is evidence that these assumptions may be invalid in cases of substantial intra-region variability (Pataky et al., in press).

An alternative approach that avoids such assumptions is to register images (Maintz and Viergever, 1998) such that homologous structures optimally overlap, and then to conduct statistical tests across the entire surface of the foot at the pixel level (Pataky and Goulermas, in press). The image processing and statistical frameworks necessary for such analyses have been established by the neuroimaging literature through a methodology called Statistical Parametric Mapping (SPM) (Friston et al., 2007). SPM was developed for the analysis of PET and fMRI data to assess the significance of cortical activity based on observable regional blood flow. Although 2D pedobarographic images and 3D functional brain images are superficially disparate, they are actually quite similar from a mathematical perspective. Both are associated with relatively constant intra-subject geometry and diverse inter-subject geometry, both analyze greyscale pixel values that reflect organ function, and, most importantly, both sample smooth continuous fields over discrete lattices. The latter point, in particular, makes both types of images ideally suited to analysis within the statistical framework of random field theory (RFT).

RFT is a branch of statistics that assesses the significance of signals observed in continuous spatial fields. The theoretical basis was originally formalized by Adler and Hasofer (Adler and Hasofer, 1976; Hasofer, 1978; Adler, 1981). Subsequent developments are attributable primarily to Friston (Friston et al., 1991; Friston et al., 1995; Friston et al., 2007, etc.) and Worsley (Worsley et al., 1992; Worsley et al., 1996, etc.) for their work in 3D functional brain imaging. RFT has also proven useful in diverse 2D imaging applications including face recognition (Chauvin et al., 2005) and astrophysics (Worsley, 1995). The main premise of RFT is that parametric statistical tests conducted at each lattice point (i.e. pixel) yield a continuous SPM that has known topological characteristics under the null hypothesis that the SPM was generated by a smooth random process. Regions of SPMs that deviate from the expected topological characteristics provide evidence of non-random processes induced by experimental manipulation. Statistical significance is then assessed by charting thresholded SPMs against topological density functions (e.g. Worsley et al., 1996).

The purposes of this study were: (1) To describe the theoretical foundation of RFT as relevant

to 2D pedobarographic imaging, (2) To assess the extent to which experimental pedobarographic data are consistent with the assumptions and expectations of RFT, and (3) To demonstrate how SPM and RFT may be used to determine the statistical significance of pedobarographic signals for purposes of scientific reporting.

2 Theory

2.1 Example SPM: the t-statistic image

Let $\boldsymbol{I}_{\mathrm{A}i}$ and $\boldsymbol{I}_{\mathrm{B}i}$ be registered peak pressure images from arbitrary experimental conditions A and B, where i and j index the number of trials (N_{A} and (N_{B}) of each condition. Mean ($\boldsymbol{M}$) and variance ($\boldsymbol{S}^2$) images are computed for condition A as:

$$\begin{aligned} \boldsymbol{M}_{\mathrm{A}} &= \tfrac{1}{N_{\mathrm{A}}} \textstyle\sum_i \boldsymbol{I}_{\mathrm{A}i} \\ \boldsymbol{S}^2_{\mathrm{A}} &= \tfrac{1}{N_{\mathrm{A}}-1} \textstyle\sum_i (\boldsymbol{I}_{\mathrm{A}i} - \boldsymbol{M}_{\mathrm{A}})^2 \end{aligned} \tag{1}$$

The t-statistic image ($\boldsymbol{SPM}\{t\}$) is:

$$\boldsymbol{SPM}\{t\} = \frac{\boldsymbol{M}_{\mathrm{A}} - \boldsymbol{M}_{\mathrm{B}}}{\sqrt{s^2_{\mathrm{p}}(1/N_{\mathrm{A}} + 1/N_{\mathrm{B}})}} \tag{2}$$

where s^2_{p} is the variance pooled over pixels and conditions (Worlsey et al. 1992).

Here the $\boldsymbol{SPM}\{t\}$ has been constructed by conducting pixel-specific t tests using a pooled variance estimate. The main problem is that a large number of t tests have been conducted; with $\alpha = 0.05$, for example, 5% of the $\boldsymbol{SPM}\{t\}$ pixels are expected to have p values lower than α simply by chance. The Bonferroni correction for multiple comparisons:

$$p_{\mathrm{critical}} = 1 - (1-\alpha)^{1/K} \tag{3}$$

where K is the number of non-zero pixels, accurately retains a family-wise error (FWE) of α if the pixel data are independent. However pedobarographic pixel data are clearly not independent because the plantar tissue is viscoelastically compliant. RFT accounts for this spatial correlation, generally increasing the critical p threshold with respect to (3). RFT procedures rely on three important concepts: field smoothness, field geometry, and binary image topology. These concepts are described in §2.2-§2.4 and are applied to statistical inference in §2.5.

2.2 Field smoothness

Field smoothness can be estimated on normalized residual images $\boldsymbol{Z}_i$:

$$\boldsymbol{Z}_i = \frac{\boldsymbol{I}_i - \boldsymbol{M}}{s_{\mathrm{p}}} \tag{4}$$

by computing the 2×2 covariance matrix $\boldsymbol{\Lambda}_k$ of the residual spatial derivatives along axes x and y:

$$\boldsymbol{\Lambda}_k = \begin{bmatrix} \mathrm{var}\left(\frac{\partial \boldsymbol{Z}_k}{\partial x}\right) & \mathrm{cov}\left(\frac{\partial \boldsymbol{Z}_k}{\partial x}, \frac{\partial \boldsymbol{Z}_k}{\partial y}\right) \\ \mathrm{cov}\left(\frac{\partial \boldsymbol{Z}_k}{\partial x}, \frac{\partial \boldsymbol{Z}_k}{\partial y}\right) & \mathrm{var}\left(\frac{\partial \boldsymbol{Z}_k}{\partial y}\right) \end{bmatrix} \tag{5}$$

where the partial derivatives are estimated using numerical approximations (e.g. Xiong et al. 1995). Here k indexes the K non-zero pixels. Global field smoothness can then be estimated by (Kiebel et al., 1999):

$$\mathrm{FWHM} = \sqrt{(4\log 2)\frac{1}{K}\sum_k |\boldsymbol{\Lambda}_k|^{-0.5}} \tag{6}$$

The FWHM metric estimates the full-width at half maximum of a Gaussian kernel that, when convolved with random field data, would produce the same smoothness as the observed residuals. Here the smoothness is estimated at each pixel and then averaged over the K non-zero pixels.

2.3 Search area geometry

The RFT-relevant 2D geometrical characteristics of irregular objects like the foot can be summarized using three parameters describing pixel connectivity (Worsley et al., 1996):

$$\begin{aligned} R_0 &= K - (E_x + E_y) + F \\ R_1 &= (E_x + E_y - 2F)/\text{FWHM} \\ R_2 &= F/\text{FWHM}^2 \end{aligned} \tag{7}$$

where E_x and E_y are the number of pairs of adjacent pixels in the x- and y-directions, respectively, and where F is the number of four-pixel squares in the search area. The R parameters define the search space up to the number of dimensions (in this case: two) and measure the area (R_2), the perimeter (R_1), and the Euler characteristic (R_0). These parameters are referred to as 'resel counts ('resolution element counts) in the literature and may be regarded as the effective number of independent observations, having accounted for smoothness.

2.4 Binary image topology

A binary image defined by threshold h and the inequality: $\boldsymbol{SPM}\{t\} > h$ contains clusters of pixels collectively referred to as the excursion set (Adler and Hasofer, 1976). Stemming from exact analytical Euler characteristic solutions (Hasofer, 1978) the excursion set has known topological properties under the null hypothesis (Hasofer, 1978; Friston et al., 1994).

2.5 Statistical inference

There are two main procedures for RFT-based statistical inference. The first is analogous to the Bonferroni correction in that it computes a corrected critical t threshold to retain a FWE of

α; all values exceeding this threshold are deemed statistically significant. This approach uses the probability that the maximum value ($t_{\max}$) of an $\boldsymbol{SPM}\{t\}$ exceeds a threshold h (Worsley et al., 1996):

$$P(t_{\max} > h) \approx \sum_{D=0}^{2} R_D \rho_D(t) \tag{8}$$

where ρ_D are Euler characteristic densities (ECDs):

$$\begin{aligned} \rho_0(t) &= \int_t^\infty \frac{\Gamma((\nu+1)/2)}{\Gamma(\nu/2)\sqrt{\nu\pi}(1+(u^2/\nu))^{-0.5(\nu+1)}}\,\mathrm{d}u \\ \rho_1(t) &= \frac{\sqrt{4\log 2}}{2\pi}\left(1+\frac{t^2}{\nu}\right)^{-0.5(v-1)} \\ \rho_2(t) &= \frac{4\log 2}{(2\pi)^{1.5}\Gamma(\nu/2)\sqrt{v/2}}\,t\left(1+\frac{t^2}{\nu}\right)^{-0.5(v-1)} \end{aligned} \tag{9}$$

Here ν is the number of degrees of freedom and Γ is the gamma function. Given a FWE of α, one may numerically compute the critical t value using (8). It is instructive to note that (8) is dependent on the geometry and smoothness of the residuals as manifested in the R parameters (7) whereas the Bonferroni correction depends only on the number of pixels. The second RFT-based inference procedure employs an arbitrary threshold h and then computes the probability that a suprathreshold cluster could have occurred by chance given its spatial extent (Friston et al. 1994). Firstly, the expected numbers of excursion set pixels (N) and clusters (m) are computed as:

$$\begin{aligned} E\{N\} &= A\rho_0(h) \\ E\{m\} &= A\rho_2(h) \end{aligned} \tag{10}$$

where A is the search area normalized by FHMW^2. The probability that the largest suprathreshold

cluster contains k or more pixels [$P(n_{\max} > k)$] is given by Friston et al. (1994):

$$\begin{aligned} P(n_{\max} > k) &= 1 - \exp(-E\{m\}e^{-\beta k}) \\ \beta &= \Gamma(2)E\{m\}/E\{N\} \end{aligned} \tag{11}$$

Note that (11) was derived for Gaussian fields, so only gives an approximate solution for t fields with high ν; more accurate results for t fields are given by Cao (1999) but are quite technical. Here (11) is retained for simplicity because the pooled variance (2) yields high effective ν.

To summarize, the first RFT inference procedure finds a critical t value based on smoothness and search area geometry and all $\boldsymbol{SPM}\{t\}$ pixels below this critical threshold are deemed insignificant. The second procedure allows one to probe the otherwise discarded sub-threshold pixels through selection of an arbitrarily lower threshold; p values are then assigned to the resulting suprathreshold clusters based on their spatial extent. This distinction is non-trivial because small but very broad signals may be deemed insignificant using the former approach. That is, (11) shows that large focal and small spatially broad signals can have identical p values (Friston et al., 1994).

3 Methods

3.1 Datasets

Three datasets were used for RFT validation (§3.2). The first was a simulated dataset consisting of 100 rectangular images of random values from the t distribution ($\nu = 8$) that approximated the dimensions of commercial pedobarographic mats (100×50 pixels) (Fig. 1A). The second dataset was identical to the first but was masked with foot-shaped geometry computed from the mean image of an experimental subject (Fig. 2A). The third dataset was experimental and consisted of twenty trials of self-paced walking for each of ten subjects (25.0±4.3 years). Pedobarographic data were sampled at 500 Hz using a 0.5 m Footscan system (RSscan, Olen, Belgium) and were continuously calibrated using force plate data (Kistler 8281B, Winterthur, Switzerland). Peak pressure images were extracted and were registered using an optimal rigid body transform (Pataky and Goulermas,

in press). Prior to participation all subjects gave informed consent according to the policies of the Research Ethics Committee of the University of Liverpool.

3.2 Validation

Three main RFT-relevant concepts were validated: FWHM estimation, variance pooling, and excursion set topological predictions. The former was validated on both the rectangular and foot-shaped random t fields. The fields were convolved with Gaussian kernels of FWHM between 1 and 100 mm (Fig. 1B-D, Fig. 2B-D) and FWHM was estimated on the resulting fields using (6) after rescaling to unit variance. Note that, because a pooled variance estimator was used to calculate $\boldsymbol{SPM}\{t\}$, smoothing the t fields is identical to smoothing the original data. This is important because RFT-relevant smoothness is an attribute of the error terms in the original data (4), not the smoothness of the $\boldsymbol{SPM}\{t\}$.

Variance pooling validation was performed on the ten-subject experimental dataset by examining the relations between pixel variance and various explanatory variables (Worlsey et al., 1992). These included: mean pressure, distance from the foot centroid, and spatial location.

Finally, RFT expectations were validated by comparing theoretical results (10) to those measured from the rectangular and foot-shaped random t fields smoothed at FWHM = 20 mm. The theoretical expectations (10) were also compared to experimental data by randomly assigning five of the twenty trials to each of conditions A and B ($\nu = 8$), computing the topological characteristics of the $\boldsymbol{SPM}\{t\}$, and repeating for 100 random assignments.

3.3 Example applications

Two previously published datasets that were originally interpreted using the Bonferroni correction (3) were re-analyzed here to: (i) Demonstrate RFT-based inference procedures, (ii) Validate previous biomechanical interpretations, and (iii) Highlight weaknesses of the Bonferroni approach. The first dataset consisted of ten trials of each of Normal and Everted walking for an example subject from Pataky and Goulermas (in press). The second set consisted of twenty trials of each of Slow, Normal, and Fast walking for an example subject from Pataky et al. (in press). The latter

study computed the $\boldsymbol{SPM}\{t\}$ using a general linear model (Friston et al., 1995); the original SPM is retained here to maintain consistency with the published data.

4 Results

4.1 Field smoothness estimation validation

FWHM estimates were very accurate on the rectangular random t fields (Fig. 1E) except for extreme field smoothness. This was expected because of numerical difficulties with gradient estimations on very rough fields (Xiong et al., 1995) and in cases when the FWHM is large with respect to the field width. For foot-shaped random fields FWHM estimates were accurate in the range 15–25 mm but substantially overestimated smoothness for FWHM $>$ 40 mm (Fig. 2E). The differences between these and the rectangular data (Fig. 1E) can be explained by the narrower foot search area. The mean experimental FWHM was 18.7$\pm$1.1 mm, within the range of good estimation.

4.2 Pooled variance validation

Standard deviation (SD) values exhibited neither systematic spatial trends (Fig. 3A, C) nor dependence on mean pixel pressure data (Fig. 3B). The low SD values observed for very low mean pressures were expected for peripheral pixels and were not considered to violate assumptions of variance pooling.

4.3 RFT prediction validation

Simulated rectangular random t fields yielded excursion set topology identical to RFT predictions (Fig. 4A). These characteristics were practically identical for foot-shaped random t fields at thresholds greater than $t = 1.5$ (Fig. 4B). Trial-to-trial experimental variability yielded t fields that were also quite consistent with RFT predictions at high t thresholds (Fig. 4C-D).

4.4 Application 1: Everted vs. normal walking

The raw $\boldsymbol{SPM}\{t\}$ comparing Everted to Normal walking was very smooth with no overlap between regions of positive and negative t values (Fig. 5A). Uncorrected, RFT-corrected, and Bonferroni-corrected excursion sets were qualitatively similar in that they all found significant increases in medial peak pressures and significant decreases in lateral peak pressures (Fig. 5B-D). The main point here is that the significance of both RFT- and Bonferroni-corrected excursion sets can only be judged en masse in a binary sense; only with the approach of Friston et al. (1994) may lower thresholds be explored by assigning p values to the individual excursion set clusters (Fig. 5E). In this case all excursion set clusters were found to be highly significant, with values notably lower than 0.05. The p value of 0.005 for the lateral heel, for example, may be interpreted as follows: given the observed field smoothness, foot geometry, and threshold $t = 0.90$, there is a 5 in 1000 chance that a statistical cluster with the same spatial extent could have occurred by chance.

4.5 Application 2: Walking speed

The raw $\boldsymbol{SPM}\{t\}$ for the walking speed data was also very smooth (Fig. 6A). The RFT-corrected excursion set (Fig. 6B) has similar biomechanical meaning to that of an arbitrary lower threshold (Fig. 6C); in both cases we may infer that the midfoot and proximal forefoot peak pressures decrease with walking speed. However the posterior midfoot effect is absent in the former. This represents a more serious limitation of thresholding using an arbitrary FWE because regions that are part of larger statistical clusters may be overlooked with high thresholds.

5 Discussion

This study has reviewed the SPM and RFT literature and has described how to determine the significance of 2D pedobarographic signals. The main new findings were that: (i) Trial-to-trial pedobarographic noise appears to be neither signal- nor location-dependent so it may be pooled into a global variance estimate, (ii) A global FWHM estimate of approximately 20 mm adequately captures the smoothness characteristics of pedobarographic fields because (iii) Using a single global

FWHM smoothness metric yields RFT predictions that are consistent with trial-to-trial variability in experimental peak pressure data.

5.1 Image smoothness

The current FWHM estimations were not perfect; estimation error was dependent on the FWHM of the underlying signal (Fig. 2E). However, the estimates were accurate in the range observed for pedobarographic data. Slight FWHM overestimation was not considered problematic for the present purposes because small errors in the FWHM have only small effects on critical RFT thresholds (Worsley, 2007) and do not cause appreciable differences between theoretical and simulated results (Fig. 4B).

The global FWHM metric (6) assumes isotropic smoothness and represents a pixel-wide average that accommodates regional smoothness variability. This stationarity assumption may not be appropriate in all cases because rough regions are more likely than smooth regions to exhibit high t values by chance. The hallux, for example, has a small contact area relative to the heel and is expected to generate signals with higher spatial frequency.

Neglecting non-stationary smoothness was presently justified because the $\boldsymbol{SPM}\{t\}$ clusters were spatially broad, spanning a large portion of the foot contact area. In $\boldsymbol{SPM}\{t\}$ fields where focal signals are observed it may be appropriate to correct for non-stationary smoothness by estimating the FWHM at each pixel and then calculating the SPM on a flattened isotropic triangular mesh (Worsley et al., 1999).

Although such correction procedures are available, it is worthwhile noting that mild spatial smoothing of the original images finesses the anisotropy / non-stationary smoothness problems, mitigating regional differences. This, in turn, makes the pooled variance assumption more plausible. Such signal conditioning has been employed previously (Pataky and Goulermas, in press; Pataky et al. in press) and is also common in neuroimaging, often mandated by inter-subject variability.

5.2 Variance pooling

There were no obvious contraindications to variance pooling over pedobarographic fields. Although pooling is not strictly necessary because ECDs may also be derived for non-pooled variance (Worsley et al. 1992), the main advantage of variance pooling is that the proportionality between mean differences and t values is maintained across the $\boldsymbol{SPM}\{t\}$. The pooled approach is presented here for simplicity and to demonstrate that pedobarographic data conform to this modelling convenience.

5.3 Theoretical and clinical implications

Using pedobarographic SPM (pSPM) and RFT for field-based statistical inference represents a departure from traditional regionalization methods. The most obvious difference is that pSPM affords a higher resolution view of pedobarographic processes of statistical interest. However, its main theoretical advantage is that it makes no anatomical assumptions regarding regional independence. Such assumptions are non-trivial because regional methods can conflate regional data, produce qualitatively erroneous results, and lead to incorrect interpretations of foot function (Pataky et al., in press). It is notable that regional conflation is inevitable when attempting to mask smooth field processes over areas with no clear local maxima. Adopting an approach like pSPM, whose spatial units (pixels) have finer resolution than the spatial processes of interest, is necessary to avoid such regional conflation.

The Bonferroni correction for multiple comparisons has been used previously (Pataky and Goulermas, in press; Pataky et al., in press) and is a valid but overly conservative approach that may hide the spatial extent of biomechanically relevant signals. Indeed, even a less extreme RFT correction may hide such effects (Fig. 6B-C). The inference procedures of Friston et al. (1994) avoid such problems by allowing arbitrarily low thresholds through cluster-specific p values, which also affords reporting convenience. For example: "the lateral forefoot exhibited significantly lower pressure in Everted vs. Normal walking ($p < 0.001$) (Fig. 5E)".

The major clinical advantage of pSPM is that entire field changes can be observed without the need for regional bar graphs or tables. This may be valuable to both the clinician and patient

because pSPMs (Fig. 5A, 6A) can be readily interpreted without any formal statistical training: red regions indicate where you have higher pressure than before surgery / than a normal subject, etc. Clinicians could also benefit from pSPM's automation: the entire analysis process, from raw data to final $\boldsymbol{SPM}\{t\}$, can occur automatically (and thus objectively) in a negligible amount of time (Pataky and Goulermas, in press).

It is acknowledged that pSPM quantifies field changes and that accurate pressure values themselves are also clinically relevant (e.g. Lavery et al., 2003). However, registering images to a common template affords efficient homologous data extraction (Pataky and Goulermas, in press), so pSPM's preprocessing procedures would also be valuable where absolute pressure values are of clinical or theoretical interest.

5.4 Future developments

The statistical maps described herein were derived from a basic t statistic after Worsley et al. (1992). Any linear statistical model is equally suitable (Friston et al., 1995), allowing for ANOVA, ANCOVA, nuisance factor modelling, parameterized experimental design, etc. The ECDs (9) change with the nature of the experimental design, with derivations also available for Gaussian, F, and χ^2 fields (Worsley et al., 1996).

Applied RFT has seen many developments in the past decade including: mixed effects modelling (Friston et al., 2005), false discovery rate (Genovese et al., 2002), regional hypotheses (Friston, 1997), non-parametric methods (Holmes et al., 1996), and Bayesian inference (Friston et al., 2002). All of these are applicable to pedobarographic data. It is hoped that the current paper will help to provide a foundation for discussion and implementation of these concepts in pedobarographic analyses.

The current paper assessed only peak pressure images, but other pedobarographic variables (e.g. contact duration, pressure impulse, etc.) are also suitable for analysis using pSPM. pSPM is also extendable to 3D pedobarographic images, where time is the third dimension. This would afford spatio-temporal hypotheses pertaining to any time instant or any span of stance phase.

5.5 Summary

Pedobarographic data are well suited to RFT analysis because of the high degree of correlation amongst neighbouring pixels. SPM-supported RFT-based statistical inference provides a convenient method for summarizing complex pedobarographic field changes in a compact and easy-to-understand visual form. pSPM appears to be a viable alternative to traditional methods that has the main theoretical advantage of maintaining field-wide objectivity through the absence of regional assumptions.

Acknowledgments

The author wishes to thank Robin H. Crompton and John Y. Goulermas for their valuable contributions to the pSPM project. Financial support was provided by the Leverhulme Trust (grant F/0025/x).

References

Adler, R. J., 1981. The Geometry of Random Fields. Wiley, New York.

Adler, R. J., Hasofer, A. M., 1976. Level crossings for random fields. Annals of Probability 4(1), 1-12.

Cao, J., 1999. The size of the connected components of excursion sets of ?2, t and F fields. Advances in Applied Probability 31(3) 579-595.

Chauvin, A., Worsley, K. J., Schyns, P. G., Arguin, M., Gosselin, F., 2005. Accurate statistical tests for smooth classification images. Journal of Vision 5, 659-667.

Friston, K. J., 1997. Testing for anatomically specified regional effects. Human Brain Mapping 5, 133-136.

Friston, K. J., Ashburner, J. T., Kiebel, S. J., Nichols, T. E., Penny, W. D. (Eds.), 2007. Statistical Parametric Mapping: The Analysis of Functional Brain Images. Elsevier, London.

Friston, K. J., Frith, C. D., Liddle, P. F., Frackowiak, R. S. J., 1991. Comparing functional (PET) images: the assessment of significant change. Journal of Cerebral Blood Flow and Metabolism 11, 690-699.

Friston, K. J., Holmes, A.P., Worsley, K. J., Poline, J. B., Frith, C. D., Frackowiak, R. S. J., 1995. Statistical parametric maps in functional imaging: a general linear approach. Human Brain Mapping 2, 189-210.

Friston, K. J., Penny, W., Phillips, C., Kiebel, S., Hinton, G., Ashburner, J., 2002. Classical and Bayesian inference in neuroimaging: theory. NeuroImage 16, 465-483.

Friston, K. J., Stephan, K. E., Lund, T. E., Morcom, A., Kiebel, S., 2005. Mixed-effects and fMRI studies. NeuroImage 24(1), 244-252.

Friston, K. J., Worsley, K. J., Frackowiak, R. S. J., Mazziotta, J. C., Evans, A. C., 1994. Assessing the significance of focal activations using their spatial extent. Human Brain Mapping 1, 210-220. Genovese, C. R., Lazar, N. A., Nichols, T. E., 2002. Thresholding of statistical maps in functional neuroimaging using the false discovery rate. Neuroimaging 15, 772-786.

Hasofer, A. M., 1978. Upcrossings of random fields. Advances in Applied Probability 10S, 14-21.

Holmes, A. P., Blair, R. C., Watson, J. D., Ford, I., 1996. Nonparametric analysis of statistic images from functional mapping experiments. Journal of Cerebral Blood Flow and Metabolism 16, 7-22.

Kiebel, S. J., Poline, J. B., Friston, K. J., Holmes, A. P., Worsley, K. J., 1999. Robust smoothness estimation in statistical parametric maps using standardized residuals from the general linear model. NeuroImage 10, 756-766.

Lavery, L. A., Armstrong, D. G., Wunderlich, R. P., Tredwell, J., Boulton, A. J. M., 2003. Predictive value of foot pressure assessment as part of a population-based diabetes disease

management program. Diabetes Care 26, 1069-1073.

Maintz, J. B. A., Viergever, M.A., 1998. A survey of medical image registration. Medical Image Analysis 2(1), 1-37.

Pataky, T. C., Caravaggi, P., Savage, R., Parker, D., Goulermas, J. Y., Sellers, W. I., Crompton, R. H., in press. New insights into the plantar pressure correlates of walking speed using pedobarographic statistical parametric mapping. Journal of Biomechanics.

Pataky, T. C., Goulermas, J. Y., in press. Pedobarographic statistical parametric mapping: a pixel-level approach to foot pressure image analysis. Journal of Biomechanics.

Rosenbaum, D., Becker, H. P., 1997. Plantar pressure distribution measurements: technical background and clinical applications. Foot and Ankle Surgery 3, 1-14.

Worsley, K. J., 1995. Boundary corrections for the expected Euler characteristic of excursion sets of random fields, with an application to astrophysics. Advances in Applied Probability 27(4), 943-959.

Worsley, K. J., 2007. Random field theory. In: Friston, K. J., et al. (Eds.), Statistical Parametric Mapping: The Analysis of Functional Brian Images. Elsevier, London, pp.232-236.

Worsley, K. J., Andermann, M., Koulis, T., MacDonald, D., Evans, A. C., 1999. Detecting changes in nonisotropic images. Human Brain Mapping 8, 98-101.

Worsley, K. J., Evans, A. C., Marrett, S., Neelin, P., 1992. A three-dimensional statistical analysis for CBF activation studies in human brain. Journal of Cerebral Blood Flow and Metabolism 12, 900-918.

Worsley, K. J., Marrett, S., Neelin, P., Vandal, A. C., Friston, K. J., Evans, A. C., 1996. A unified statistical approach for determining significant signals in image of cerebral activation. Human Brain Mapping 4, 58-73.

Xiong J., Gao, J. H., Lancaster, J. L., Fox, P. T., 1995. Clustered pixels analysis for functional MRI activation studies of the human brain. Human Brain Mapping 3, 287-301.

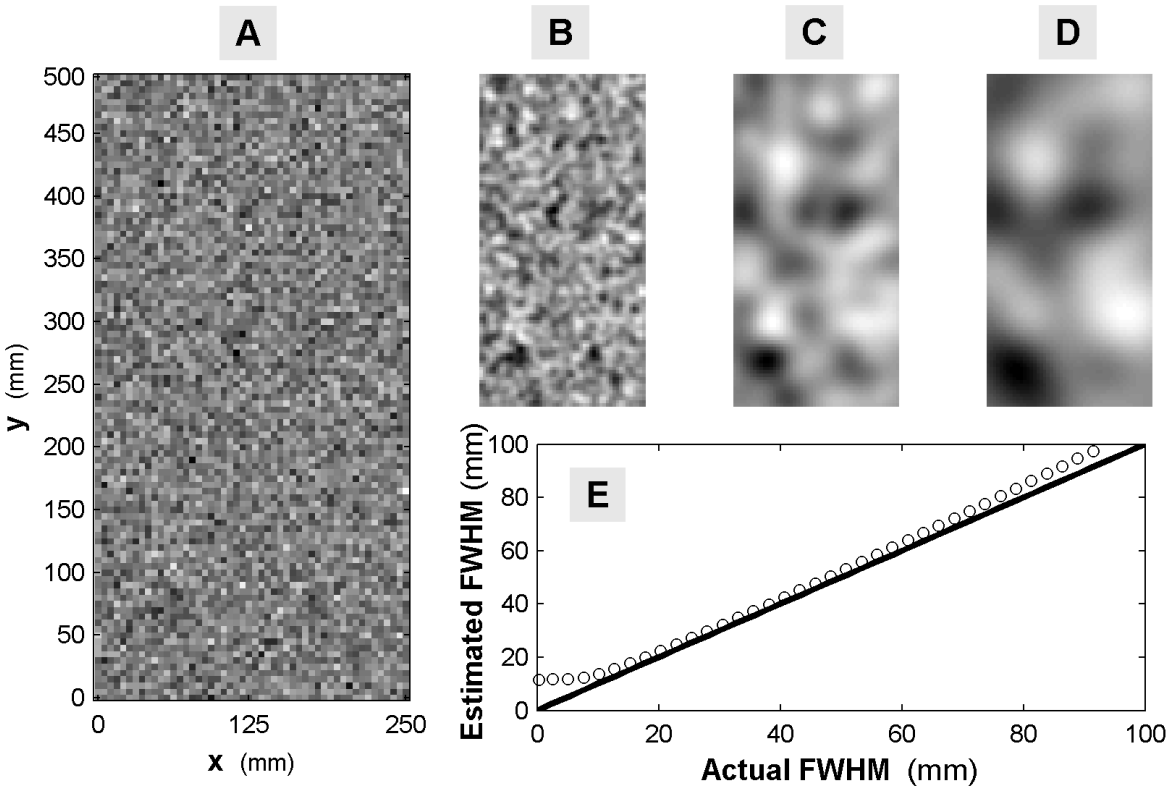

Figure 1. Validation of *FWHM* estimation. (A) A random 100×50 pixel *t* field ($\nu = 8$) with dimensions approximating a pedobarographic mat (sensor area: 5 mm^2). The image in (A) was smoothed in panels (B)-(D) with Gaussian kernels of *FWHM* = 10, 50, and 90 mm, respectively. Image values have been scaled such that minimum and maximum values are black and white, respectively. (E) Comparison between actual (thick black line) and numerically estimated *FWHM* (open circles). These estimates are averaged over 100 random images like (A).

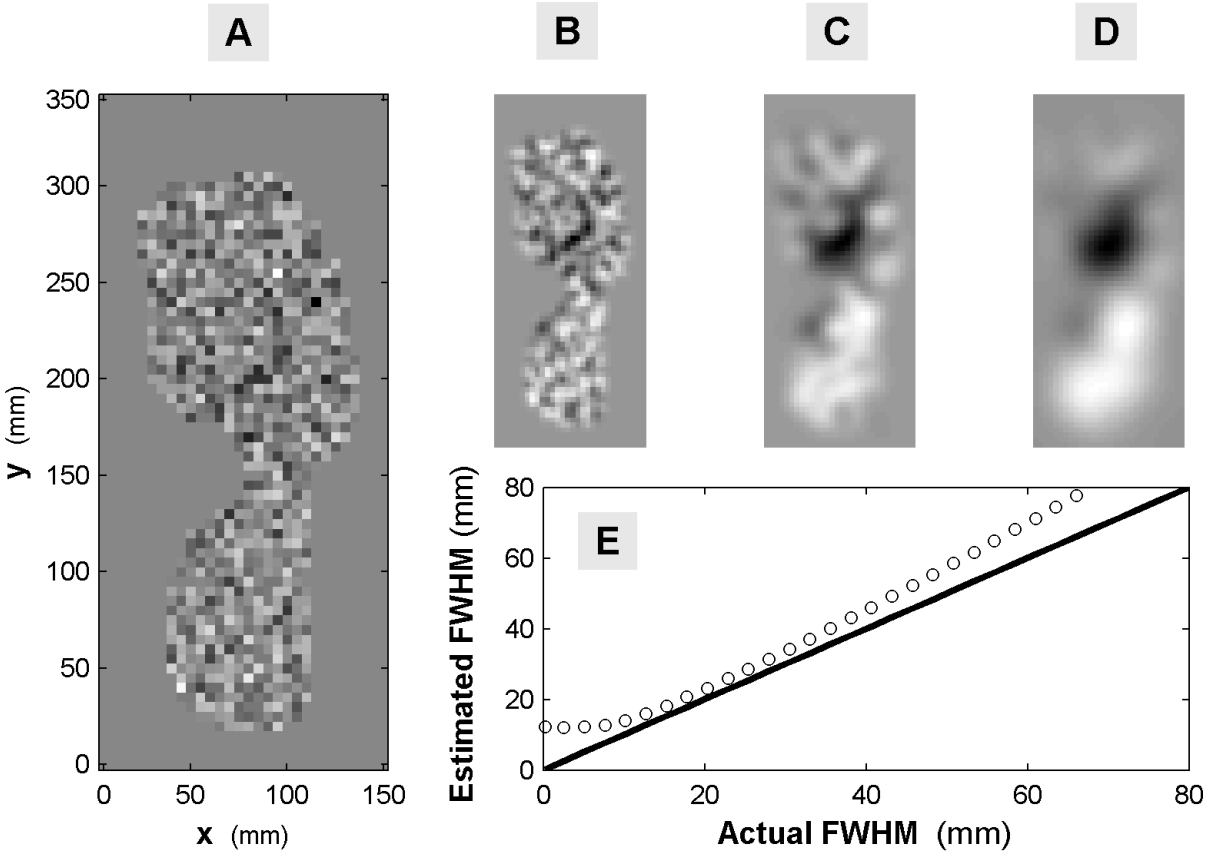

Figure 2. Validation of *FWHM* estimation for foot-shaped random fields; the foot shape was derived from the mean image for a single subject. Data are presented as for Fig. 1 except here panels (B)-(D) contain images that have been smoothed with Gaussian kernels of *FWHM* = 10, 25, and 40 mm, respectively.

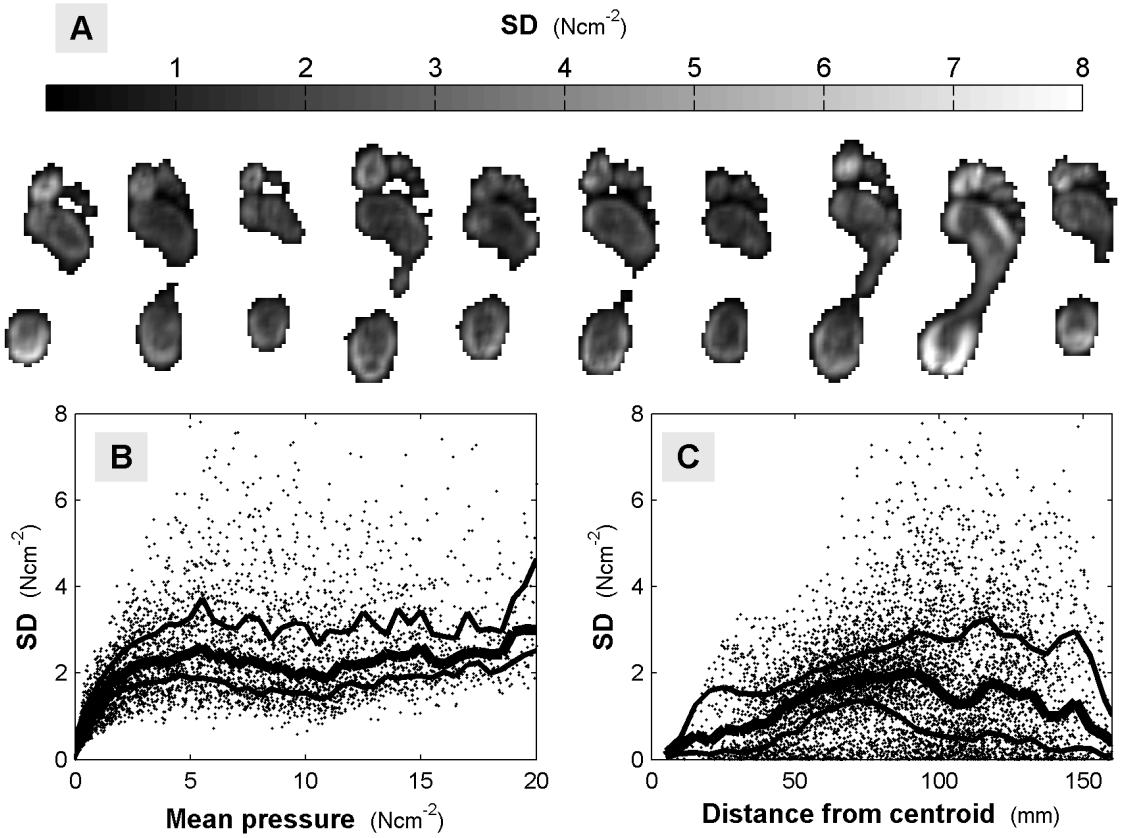

Figure 3. Validation of variance pooling. (A) Standard deviation (SD) images for the ten experimental subjects. (B) SD vs. mean pressure. (C) SD as a function of the distance from the foot image centroid. The thick and thin lines in (B) and (C) indicate the median and upper/lower quartiles, respectively.

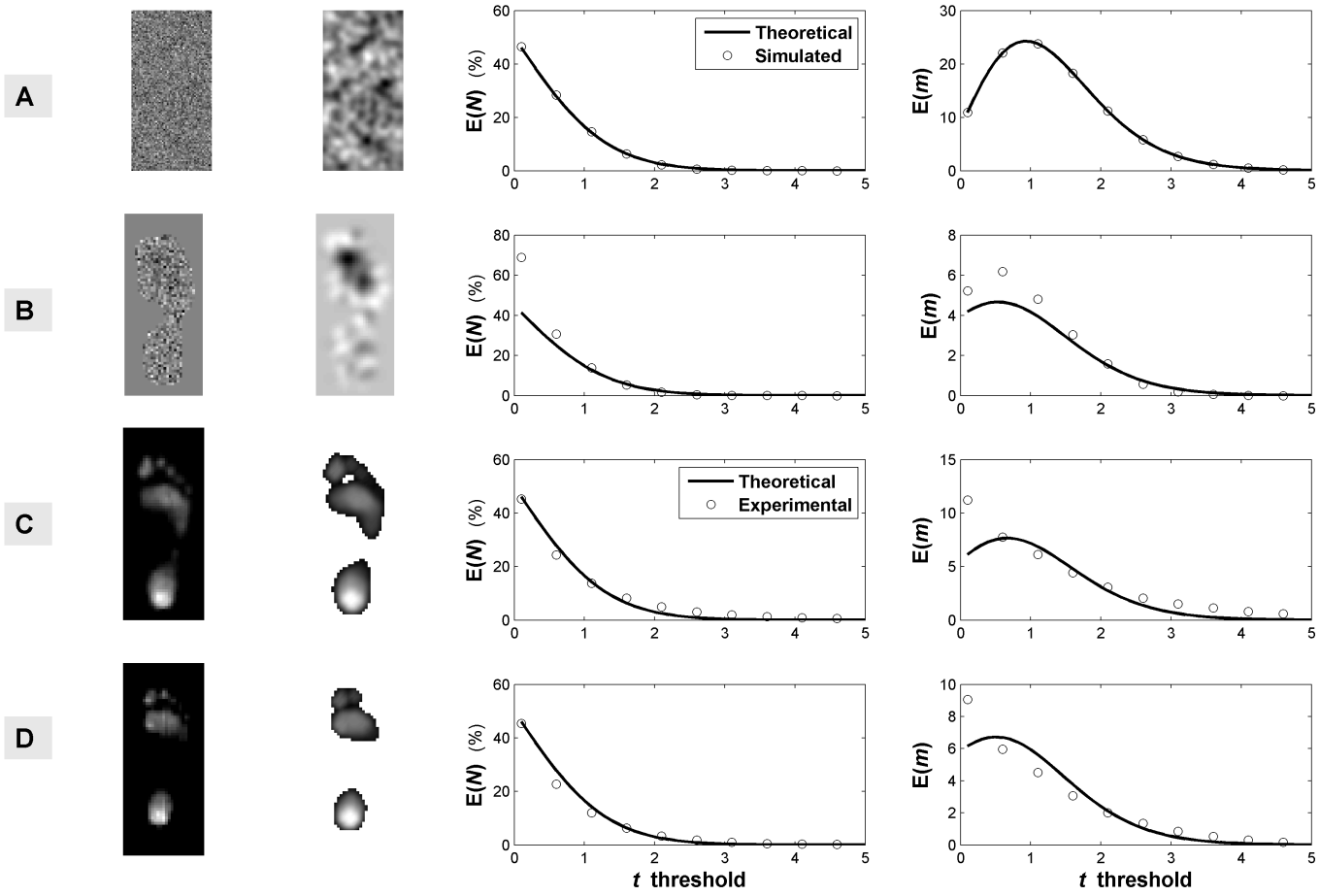

Figure 4. Validation of RFT predictions regarding excursion set topology. (A) Random *t* field with column panels illustrating a raw image, a smoothed image, the expected percentage of pixels (E(*N*)) greater than threshold *t*, and the expected number of clusters (E(*m*)) in the excursion set, respectively. (B) Random foot-shaped *t* field. (C) Experimental results from a single subject. (D) Experimental results from a high-arched subject. Solid lines indicate theoretical predictions. Open circles indicate simulated results in (A) and (B) and experimental results in (C) and (D).

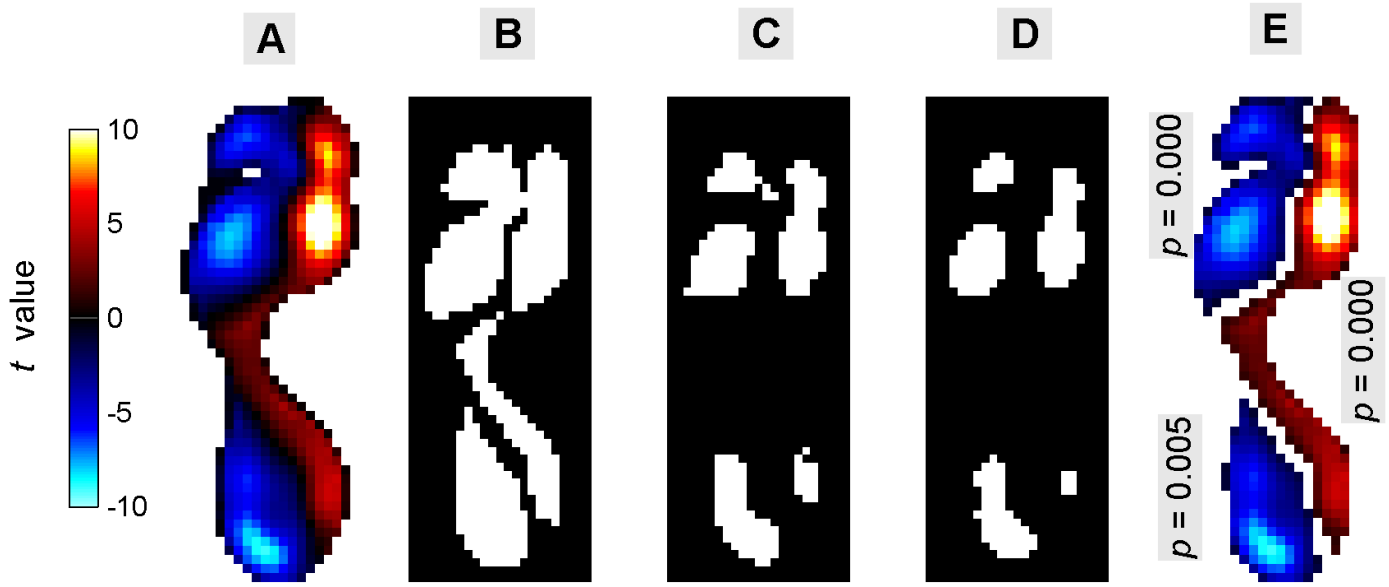

Figure 5. Example application: everted walking. (A) Raw ***SPM***{*t*} showing where Everted walking peak pressures were associated with higher (warm colours) and lower (cool colours) peak pressures as compared to Normal walking. (B) Excursion set for an uncorrected threshold of $p = 0.05$, $t = 1.73$. (C) Excursion set for a RFT corrected threshold of $p = 0.05$, $t = 4.24$. (D) Excursion set for a Bonferroni-corrected $p = 5\times10^{-5}$, $t = 4.80$. (E) RFT-based p values for excursion set clusters using an arbitrary threshold of $t = 0.90$.

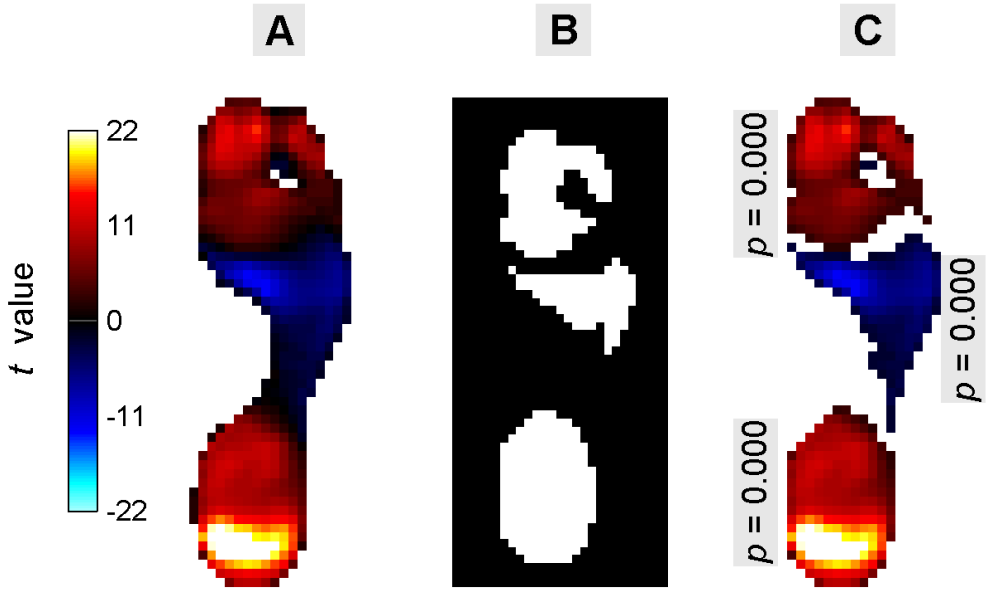

Figure 6. Example application: walking speed. (A) Raw ***SPM***{*t*} showing where peak pressures correlated positively (warm colours) and negatively (cool colours) with walking speed. (B) Excursion set for a RFT-corrected threshold of $p = 0.05$, $t = 3.77$. (C) RFT-based p values for excursion set clusters using a threshold of $t = 2.0$.